3D Nitrogen–Doped Graphene Aerogel–Supported Fe3O4 Nanoparticles as Efficient Electrocatalysts for the Oxygen Reduction Reaction

Journal:	*Journal of the American Chemical Society*
Manuscript ID:	ja-2012-030565.R1
Manuscript Type:	Communication
Date Submitted by the Author:	22-May-2012
Complete List of Authors:	Wu, Zhong-Shuai; Max-Planck-Institut für Polymerforschung, Synthetic Chemistry Yang, Shubin; Max-Planck-Institut für Polymerforschung, Sun, Yi; Max-Planck-Institut für Polymerforschung, Parvez, Khaled; Max Planck Institute for Polymer Research, Feng, Xinliang; Max-Planck Institute for Polymer Research, Synthetic Chemistry Mullen, Klaus; Max-Planck-Institute for Polymer Research,

3D Nitrogen–Doped Graphene Aerogel–Supported Fe$_3$O$_4$ Nanoparticles as Efficient Electrocatalysts for the Oxygen Reduction Reaction

Zhong–Shuai Wu, Shubin Yang, Yi Sun, Khaled Parvez, Xinliang Feng,* and Klaus Müllen*

Max-Planck-Institut für Polymerforschung, Ackermannweg 10, 55128 Mainz, Germany

Supporting Information

ABSTRACT: Three–dimensional nitrogen–doped graphene aerogel–supported Fe$_3$O$_4$ nanoparticles (Fe$_3$O$_4$/N–GAs) as efficient cathode catalysts for the oxygen reduction reaction (ORR) is reported. The graphene hybrids exhibit an interconnected macroporous framework of graphene sheets with uniform dispersion of Fe$_3$O$_4$ nanoparticles. In studying the carbon support effects on the Fe$_3$O$_4$ nanoparticles for ORR, we find that Fe$_3$O$_4$/N–GAs shows more positive onset potential, higher cathodic density, lower H$_2$O$_2$ yield and higher electron transfer number for ORR in alkaline medium than Fe$_3$O$_4$–supported on N–doped carbon black or on N–doped graphene sheets, highlighting the importance of 3D macropores and high specific surface area of graphene aerogel support for improving the ORR performance. Furthermore, Fe$_3$O$_4$/N–GAs shows better durability than the commercial Pt/C catalyst.

Catalysts for the oxygen reduction reaction (ORR) are key components of fuel cells.[1] Pt and its alloys remain the most efficient ORR catalysts, but the high cost and scarcity of Pt hamper further development of fuel cell technologies based on these materials. In this respect, a broad range of alternative catalysts based on non–precious metals (Fe, Co, etc)[2] or oxides (Fe$_2$O$_3$, Fe$_3$O$_4$, Co$_3$O$_4$, IrO$_2$ etc),[3] as well as nitrogen-coordinated metal on carbon,[4] and metal–free doped carbon materials[5] have been actively pursued. Metal or metal oxide catalysts frequently suffer from dissolution, sintering and agglomeration during the fuel cell operation which can result in catalyst degradation.[6] To overcome this obstacle, nanostructured catalyst supports such as carbon (active carbon, porous carbon, carbon nanotube and graphene), metal, carbide, mesoporous silica and conducting polymers have been developed to maximize the electro–active surface area of catalysts and improve their catalytic activity and durability.[6] Among these, graphene, a two–dimensional single–layer sheet of hexagonal carbon, has emerged as a new generation catalyst support due to its excellent electrical conductivity, high surface area, good chemical and environmental stability, and strong adhesion to catalyst particles. Despite the tremendous progress of graphene–based catalysts for ORR,[3e,7] there has been no report of the controllable assembly of non–precious metal oxide nanoparticles (NPs) supported on a three–dimensional (3D) graphene network as ORR catalysts. Such systems are attractive targets as they allow the unique features of graphene sheets, such as rich macroporosity and multi–dimensional electron transport partway to be utilized.

In this communication, we demonstrate a novel class of monolithic Fe$_3$O$_4$ NPs supported on 3D nitrogen–doped graphene aerogels (Fe$_3$O$_4$/N–GAs). The graphene hybrids show an interconnected macroporous framework of graphene sheets with uniform deposition of Fe$_3$O$_4$ NPs. In studying the carbon support effects on the Fe$_3$O$_4$ NP ORR catalyst, we find that Fe$_3$O$_4$/N–GAs exhibits a more positive onset potential, a higher cathodic density, a lower H$_2$O$_2$ yield and a higher electron transfer number for ORR in alkaline condition than Fe$_3$O$_4$–supported on N–doped carbon black (Fe$_3$O$_4$/N–CB) or on N–doped graphene sheets (Fe$_3$O$_4$/N–GSs). Additionally, Fe$_3$O$_4$/N–GAs shows better durability than the commercial Pt/C catalyst.
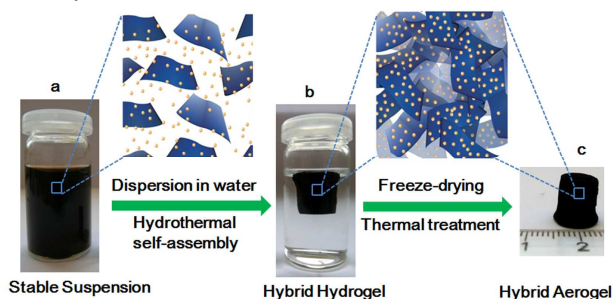

Figure 1. Fabrication process for a 3D Fe$_3$O$_4$/N–GAs catalyst. (a) A stable suspension of GO, iron ions and polypyrrole (PPy) are dispersed in a vial. (b) Fe– and PPy–supported graphene hybrid hydrogel prepared by hydrothermal self-assembly and floated on water in a vial, and its ideal assembled model. (c) A monolithic hybrid aerogel of Fe$_3$O$_4$/N–GAs obtained after freeze–drying and thermal treatment.

The fabrication process for 3D Fe$_3$O$_4$/N–GAs is demonstrated in Figure 1. First, graphene oxide (GO, Figure S1 in Supporting Information)[8] was dispersed in water by sonication reaching a concentration up to 1.5 mg mL^{-1}. Afterwards, iron acetate (1~40 mg) and PPy (20 mg) were slowly added into 6 mL GO dispersion to form a stable aqueous suspension (Figure 1a). Subsequently, these ternary components were hydrothermally assembled to form a 3D

graphene–based hydrogel at 180 °C for 12 h (Figure 1b). In this way, Fe_3O_4 NPs could nucleate and grow on the graphene surface while simultaneously incorporating nitrogen species into the graphene lattice. The as–prepared hydrogel was then directly dehydrated via a freeze–drying process to maintain the 3D monolithic architecture and then heated at 600 °C for 3 h under nitrogen (Figure 1c). The final product from this process was a black monolithic hybrid aerogel comprised of N–doped graphene networks and Fe_3O_4 NPs (see below).
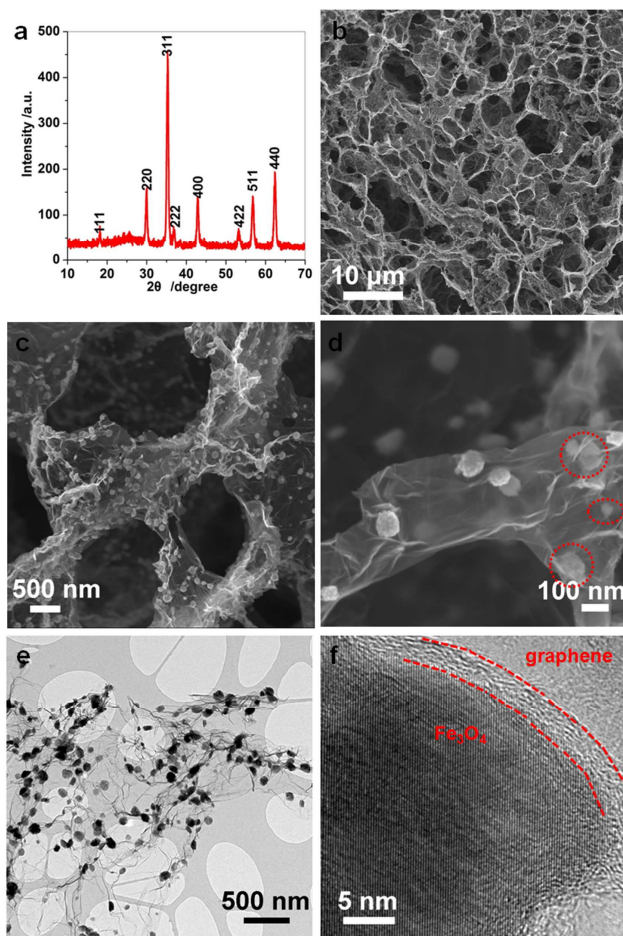

Figure 2. Structure and morphology of Fe_3O_4/N–GAs catalysts. (a) XRD pattern and, (b–d) Typical SEM images of Fe_3O_4/N–GAs reveal the 3D macroporous structure and uniform distribution of Fe_3O_4 nanoparticles in the graphene aerogel. Red rings indicate that Fe_3O_4 NPs are encapsulated in thin graphene layers. (e) Representative TEM and (f) HRTEM images of Fe_3O_4/N–GAs reveal a wrapped structure of Fe_3O_4 NP by graphene layers.

The structure and morphology of as–prepared Fe_3O_4/N–GAs were investigated by means of X–ray diffraction (XRD), scanning (SEM) and transmission (TEM) electron microscopy. The XRD pattern confirms the formation of Fe_3O_4 (JCPDS No. 65–3107) in the hybrids (Figure 2a).[9] Remarkably, no apparent diffraction peak can be identified in the range of 20~30°, indicating that Fe_3O_4 NPs have been efficiently deposited on the graphene surface suppressing the stacking of graphene layers. SEM images reveal an interconnected 3D porous graphene framework with continuous macropores in the micrometer size range (Figure 2b and c). Apart from the decoration of Fe_3O_4 NPs on both sides of graphene sheets

(Figure 2c), it is noteworthy that a significant portion (30% based on statistical analysis of SEM images) of NPs are encapsulated within graphene layers (Figure 2d), suggesting an efficient assembly between NPs and graphene sheets. Such a geometric confinement of metal oxide NPs within graphene layers has been reported to enhance their interface contact and to suppress the dissolution and agglomeration of NPs, and in this way to promote the electrochemical activity and stability of hybrids.[10] TEM characterization further validates the uniform distribution of Fe_3O_4 NPs with a size of 20–80 nm on graphene (Figure 2e). The high–resolution TEM (HRTEM) image reveals that a typical Fe_3O_4 NP with a well–crystalline texture is entirely encapsulated by graphene sheets (≤6 layers, Figure 2f). The Brunauer–Emmett–Teller (BET) analysis shows that a specific surface area of 110 $m^2 g^{-1}$ for Fe_3O_4/N–GAs together with meso– and macroporous features can be obtained (Figure S2). The content of Fe_3O_4 in Fe_3O_4/N–GAs was further confirmed by thermogravimetric analysis (46.2 wt%, Figure S3).
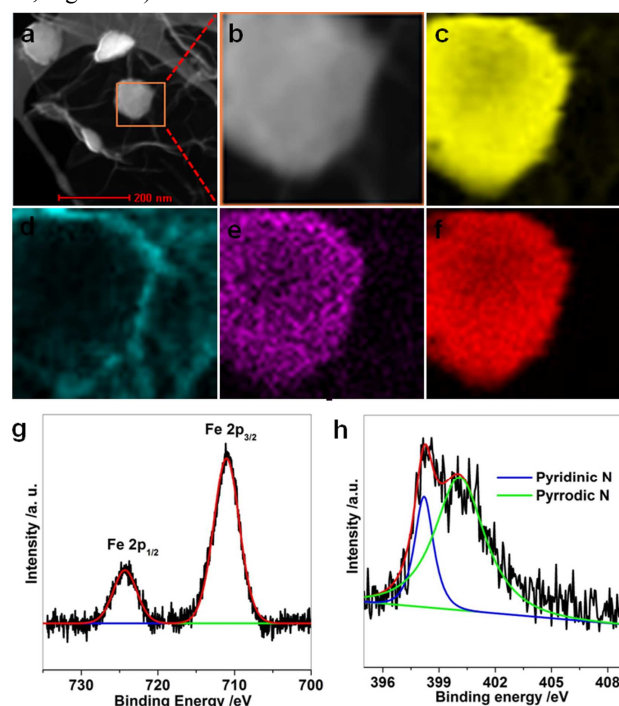

Figure 3. Elemental mapping images and XPS of Fe_3O_4/N–GAs. (a) Typical scanning transmission electron microscopy (STEM) image, (b) STEM image taken from the square region in (a) and corresponding elemental mapping images of (c) iron, (d) carbon, (e) nitrogen, and (f) oxygen in (b). (g, h) High-resolution (g) Fe 2p XPS and (h) N 1s XPS of Fe_3O_4/N–GAs.

Elemental mapping analysis of Fe_3O_4/N–GAs suggests the presence of Fe, C, N and O components in the hybrids (Figure 3af). It is notable that the nitrogen content is much higher in the region of Fe_3O_4 NPs than in graphene layers (Figure 3e), indicating that Fe–N–C active sites have been established at the Fe_3O_4 NP interface. X–ray photoelectron spectroscopy (XPS, Figure 3g and Figure S4) shows two peaks at 725 and 711 eV, assignable to Fe $2p_{1/2}$ and Fe $2p_{3/2}$ for Fe_3O_4, respectively.[9] Further, 3.5 wt% nitrogen can be estimated to be present in these hybrids based on XPS analysis. The high–resolution scan of N 1s indicates the presence of two forms of

nitrogen, namely, pyrrolic N (401.2 eV) and pyridinic N (398.1 eV, Figure 3h),[11] both of which have proven to be the catalytically active sites for oxygen reduction.[12]

To gain insight into the ORR of Fe_3O_4 NPs supported on the 3D macroporous N–GAs, we first examined the electrocatalytic properties of Fe_3O_4/N–GAs using cyclic voltammetry in nitrogen– and oxygen–saturated 0.1 M KOH aqueous electrolyte solution at a scan rate of 100 mV s^{-1} (Figure 4a). For comparison, we also prepared Fe_3O_4 NPs loaded on other carbon supports such as N–doped graphene sheets (Fe_3O_4/N–GSs) and carbon black (Fe_3O_4/N–CB) via the same procedure (Supporting Information, Figure S5–S8). In the case of an argon–saturated solution, CV curves within the potential range of –1.2~+0.2 V present similar features for all three samples. A small redox response could be observed at –0.5~–0.7 V, attributable to the pseudocapacitive behavior of nitrogen-doped carbons (Figure 4a, Figure S6).[13] In contrast, when the electrolyte was saturated with oxygen, three electrodes showed a substantial reduction process. Apparently, Fe_3O_4/N–GAs exhibited a pronounced electrocatalytic activity for ORR associated with a more positive ORR onset potential (–0.19 V) and higher cathodic current density (–2.56 mA cm^{-2}, Figure 4a) than in the case of Fe_3O_4/N–GSs (–0.26 V, –1.46 mA cm^{-2}, Figure S6a) and Fe_3O_4/N–CB (–0.24 V, –1.99 mA cm^{-2}, Figure S6b). Subsequently, rotating disk electrode (RDE) was performed to examine the reaction kinetics for Fe_3O_4/N–GAs, Fe_3O_4/N–GSs and Fe_3O_4/N–CB electrodes in O_2–saturated 0.1 M KOH electrolyte at a scan rate of 10 mV s^{-1} (Figure 4b, Figure S6). Two–step reaction pathways could be observed for Fe_3O_4/N–GSs (from –0.26 to –0.62 V and from –0.62 to –1.2 V, Figure S6c) and Fe_3O_4/N–CB (from –0.24 V to –0.60 V and from –0.60 to –1.2 V, Figure S6d), suggesting the key role of a two–electron transfer to produce hydrogen peroxide anions (HO_2^-) as intermediates in alkaline medium. In contrast, the linear sweep voltammetry (LSV) curves of Fe_3O_4/N–GAs presents a direct four-electron transfer pathway from –0.19 to –1.2 V for producing hydroxide (OH^-) (Figure 4b).
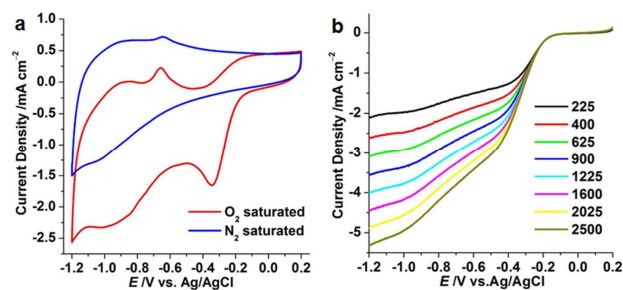

Figure 4. (a) Cyclic voltammetry curves of Fe_3O_4/N–GAs in nitrogen– and oxygen–staturated 0.1 M KOH aqueous electrolyte solution. The scan rate is 100 mV s^{-1}. (b) LSV curves of Fe_3O_4/N–GAs in an oxygen–saturated 0.1 M KOH at a scan rate of 10 mV s^{-1} and different rotation rates, recorded by RDE voltammograms.

We further employed a rotating ring–disk electrode (RRDE) technique to quantify the ORR electron transfer pathway, in which the amount of H_2O_2 generated at the disk electrode could be accurately determined.[12] Figure 5a shows the disk and ring currents for Fe_3O_4/N–GAs, Fe_3O_4/N–GSs, and

Fe_3O_4/N–CB, respectively. All three electrodes generated ring currents at the onset potential for ORR. Notably, both Fe_3O_4/N–GSs and Fe_3O_4/N–CB exhibit much higher ring currents than that of Fe_3O_4/N–GAs (Inset in Figure 5a). Specifically, the measured H_2O_2 yield for Fe_3O_4/N–GAs is 11% at the potential of –0.4 V, while that for Fe_3O_4/N–GSs is 45%, and for Fe_3O_4/N–CB is 38%, respectively (Figure 5b). Figure 5c reveals that the electron transfer number strongly varies with the measured potential. Based on the ring and disk current, the electron transfer number is 3.09~3.80 for Fe_3O_4/N–GSs and 3.24~3.80 for Fe_3O_4/N–CB in a potential range from –0.20 to –1.2 V. In sharp contrast, the *n* value of Fe_3O_4/N–GAs electrode lies between 3.72 to 3.95 over the whole potential range, emphasizing that the Fe_3O_4/N–GAs ORR proceeds mainly via a four–electron mechanism. Taking into account the similar elemental compositions of the three samples, the enhanced ORR activity of Fe_3O_4/N–GAs can be attributed to the effect of macropores on the diffusion rate of the electrolyte and to the exposed active sites, which are closely related to its high BET surface area (Figure S2) relative to that of Fe_3O_4/N–GSs (Figure S7) and Fe_3O_4/N–CB (Figure S8).
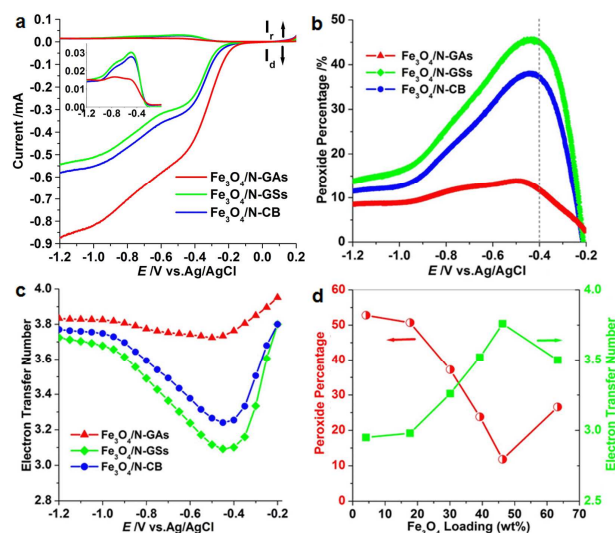

Figure 5. (a) RRDE test of ORR on Fe_3O_4/N–GAs, Fe_3O_4/N–GSs, Fe_3O_4/N–CB in oxygen-saturated 0.1 M KOH electrolyte at a rotation rate of 1600 rpm. Inset is the ring current as a function of the electrode potential. (b) Percentage of peroxide and (c) the electron transfer number (*n*) of Fe_3O_4/N–GAs, Fe_3O_4/N–GSs, and Fe_3O_4/N–CB against the electrode potential. (d) Percentage of peroxide and electron transfer number as a function of Fe_3O_4 loading at –0.4 V, measured by RRDE in an O_2–saturated 0.1 M KOH electrolyte.

The durability of Fe_3O_4/N–GAs with respect to commercial Pt/C was assessed through chronoamperometric measurements at –0.4 V in O_2 saturated aqueous solution of 0.1 M KOH at a rotation rate of 1600 rpm. As revealed in Figure S9, the current–time (i–t) chronoamperometric response for Fe_3O_4/N–GAs exhibited a very slow attenuation with a high current retention (79.3%) after 20000 s. In contrast, a commercial Pt–C electrode showed a much faster current decrease with ~61.0% retention. The better durability of Fe_3O_4/N-GAs can be ascribed to the unique confined structure of Fe_3O_4 NPs within graphene layers (Figure 2b-f), which can enhance their

interfacial contact, suppress the dissolution/agglomeration of NPs, and facilitate the transport of electrolyte ions.[10] The influence of the Fe_3O_4 NP loading on the catalytic activity of Fe_3O_4/N–GAs was also examined by RRDE. Figure 5d demonstrates that with increasing Fe_3O_4 loading from about 4.1 to 46.2 wt% in Fe_3O_4/N–GAs, the yield of HO_2^- decreases and the overall electron transfer number increases from 2.9 to 3.8. However, a high Fe_3O_4 loading of 63.3 wt% in these hybrid results in an increase of HO_2production. This can be explained by (i) the decrease of the electrical conductivity of the Fe_3O_4/N–GAs electrode upon increasing the Fe_3O_4 loading, and (ii) the onset of non–bonded interactions with N–GAs for the excessive Fe_3O_4 NPs.

Furthermore, we found that 3D N-GAs is also a universal carbon support, which is superior to other carbon supports of GSs and CB, for loading non-precious metal electrocatalysts. For example, Fe NPs were also successfully incorporated into N-GAs, which show remarkable ORR performance in acidic medium (Figure S10-S14, and Table S1).

In summary, we have successfully fabricated 3D monolithic Fe_3O_4/N–GAs hybrids via a combined hydrothermal self–assembly, freeze–drying and thermal treatment process. Due to the 3D macroporous structure and high surface area, the resulting Fe_3O_4/N–GAs show excellent electrocatalytic activity for ORR in alkaline electrolytes, including higher current density, lower ring current, lower H_2O_2 yield, higher electron transfer number (~4), and better durability, which makes Fe_3O_4/N–GAs a potentially non–precious metal cathode catalyst for fuel cells. We believe that our present synthetic strategy can be further extended to develop other 3D metal or metal oxide/graphene–based monolithic materials for various applications, such as sensors, batteries, and supercapacitors.

■ ASSOCIATED CONTENT

Supporting Information
Full synthesis and characterization details, AFM image of graphene oxide, nitrogen cryosorption isotherm and pore distribution, TGA and XPS of Fe_3O_4/N–GAs, SEM images, CV, LSV curves, nitrogen cryosorption isotherm and pore distribution of Fe_3O_4/N–GSs and Fe_3O_4/N–CB, durability of Fe_3O_4/N–GAs and Pt/C in alkaline solution. XRD, SEM, TEM, EDX and RRDE curves of Fe/N-GAs, Fe/N-GAs and Fe/N-CB, durability of Fe/N–GAs and Pt/C in acidic solution. This material is available free of charge via the Internet at http://pubs.acs.org.

■ AUTHOR INFORMATION

Corresponding Author
feng@mpip–mainz.mpg.de; muellen@mpip–mainz.mpg.de
Notes
The authors declare no competing financial interest.

■ ACKNOWLEDGMENT

■ REFERENCES

(1) (a) Bashyam, R.; Zelenay, P. *Nature* **2006**, *443*, 63; Lefevre, M.; (b) Proietti, E.; Jaouen, F.; Dodelet, J. P. *Science* **2009**, *324*, 71; (c) Wu, G.; More, K. L.; Johnston, C. M.; Zelenay, P. *Science* **2011**, *332*, 443.

(2) (a) Jaouen, F.; Proietti, E.; Lefevre, M.; Chenitz, R.; Dodelet, J. P.; Wu, G.; Chung, H. T.; Johnston, C. M.; Zelenay, P. *Energy Environ. Sci.* **2011**, *4*, 114; (b) Bezerra, C. W. B.; Zhang, L.; Lee, K. C.; Liu, H. S.; Marques, A. L. B.; Marques, E. P.; Wang, H. J.; Zhang, J. J. *Electrochim. Acta* **2008**, *53*, 4937; (c) Morozan, A.; Jousselme, B.; Palacin, S. *Energy Environ. Sci.* **2011**, *4*, 1238; (d) Su, D. S.; Sun, G. Q. *Angew. Chem. Int. Ed.* **2011**, *50*, 11570.

(3) (a) Zhou, W.; Ge, L.; Chen, Z. G.; Liang, F. L.; Xu, H. Y.; Motuzas, J.; Julbe, A.; Zhu, Z. H. *Chem. Mater.* **2011**, *23*, 4193; (b) Vago, E. R.; Calvo, E. J. *J. Chem. Soc. Faraday Trans.* **1995**, *91*, 2323; (c) Medard, C.; Lefevre, M.; Dodelet, J. P.; Jaouen, F.; Lindbergh, G. *Electrochim. Acta* **2006**, *51*, 3202; (d) Choi, C. H.; Lee, S. Y.; Park, S. H.; Woo, S. I. *Appl. Catal. B-Environ.* **2011**, *103*, 362; (e) Liang, Y. Y.; Li, Y. G.; Wang, H. L.; Zhou, J. G.; Wang, J.; Regier, T.; Dai, H. J. *Nature Mater.* **2011**, *10*, 780; (f) Chang, C. H.; Yuen, T. S.; Nagao, Y.; Yugami, H. *Solid State Ionics* **2011**, *197*, 49; (g) Chang, C. H.; Yuen, T. S.; Nagao, Y.; Yugami, H. *J. Power Sources* **2010**, *195*, 5938.

(4) (a) Liu, R. L.; von Malotki, C.; Arnold, L.; Koshino, N.; Higashimura, H.; Baumgarten, M.; Müllen, K. *J. Am. Chem. Soc.* **2011**, *133*, 10372; (b) Charreteur, F.; Jaouen, F.; Ruggeri, S.; Dodelet, J. P. *Electrochim. Acta* **2008**, *53*, 2925; (c) Morozan, A.; Campidelli, S.; Filoramo, A.; Jousselme, B.; Palacin, S. *Carbon* **2011**, *49*, 4839; (d) Chang, C. J.; Deng, Y. Q.; Shi, C. N.; Chang, C. K.; Anson, F. C.; Nocera, D. G. *Chem. Commun.* **2000**, 1355; (e) Chang, C. J.; Loh, Z. H.; Shi, C. N.; Anson, F. C.; Nocera, D. G. *J. Am. Chem. Soc.* **2004**, *126*, 10013.

(5) (a) Liu, R. L.; Wu, D. Q.; Feng, X. L.; Müllen, K. *Angew. Chem. Int. Ed.* **2010**, *49*, 2565; (b) Wang, S. Y.; Yu, D. S.; Dai, L. M.; Chang, D. W.; Baek, J. B. *ACS Nano* **2011**, *5*, 6202; (c) Li, Y.; Zhao, Y.; Cheng, H.; Hu, Y.; Shi, G. Q.; Dai, L. M.; Qu, l. T. *J. Am. Chem. Soc.* **2012**, *134*, 15; (d) Wang, S.; Iyyamperumal, E.; Roy, A.; Xue, Y.; Yu, D.; Dai, L. M. *Angew. Chem. Int. Ed.* **2011**, *50*, 11756.

(6) Wang, Y. J.; Wilkinson, D. P.; Zhang, J. J. *Chem. Rev.* **2011**, *111*, 7625.

(7) (a) Jafri, R. I.; Rajalakshmi, N.; Ramaprabhu, S. *J. Mater. Chem.* **2010**, *20*, 7114; (b) Wang, H. L.; Liang, Y. Y.; Li, Y. G.; Dai, H. J. *Angew. Chem. Int. Ed.* **2011**, *50*, 10969; (c) Seo, M. H.; Choi, S. M.; Kim, H. J.; Kim, W. B. *Electrochem. Commun.* **2011**, *13*, 182; (d) Li, Y.; Wang, H.; Xie, L.; Liang, Y.; Hong, G.; Dai, H. *J. Am. Chem. Soc.* **2011**, *133*, 7296; (e) Li, Y.; Wang, H.; Zhou, J.; Li, Y.; Wang, J.; Regier, T.; Dai, H. *J. Am. Chem. Soc.* **2012**, *134*, 3517; (f) Yan, X. Y.; Tong, X. L.; Zhang, Y. F.; Han, X. D.; Wang, Y. Y.; Jin, G. Q.; Qin, Y.; Guo, X. Y. *Chem. Commun.* **2012**, *48*, 1892; (g) Wu, J. J.; Zhang, D.; Wang, Y.; Wan, Y.; Hou, B. R. *J. Power Sources* **2012**, *198*, 122; (h) Guo, S.; Sun, S. *J. Am. Chem. Soc.* **2012**, *134*, 2492.

(8) (a) Liang, Y.; Wu, D.; Feng, X.; Müllen, K. *Adv. Mater.* **2009**, *21*, 1679; (b) Yang, S. B.; Feng, X. L.; Wang, L.; Tang, K.; Maier, J.; Müllen, K. *Angew. Chem. Int. Ed.* **2010**, *49*, 4795.

(9) Chen, W. F.; Li, S. R.; Chen, C. H.; Yan, L. F. *Adv. Mater.* **2011**, *23*, 5679.

(10) (a) Yang, S. B.; Feng, X. L.; Ivanovici, S.; Müllen, K. *Angew. Chem. Int. Ed.* **2010**, *49*, 8408; (b) Chen, D. Y.; Ji, G.; Ma, Y.; Lee, J. Y.; Lu, J. M. *ACS Appl. Mater. Inter.* **2011**, *3*, 3078.

(11) Wu, Z. S.; Ren, W. C.; Xu, L.; Li, F.; Cheng, H. M. *ACS Nano* **2011**, *5*, 5463.

(12) Gong, K. P.; Du, F.; Xia, Z. H.; Durstock, M.; Dai, L. M. *Science* **2009**, *323*, 760.

(13) Yang, W.; Fellinger, T. P.; Antonietti, M. *J. Am. Chem. Soc.* **2011**, *133*, 206.

Table of Contents (TOC) Graphic